The Astrophysical Journal Letters, 881:L30 (7pp), 2019 August 20 https://doi.org/10.3847/2041-8213/ab365f

Solar Image Restoration with the CycleGAN Based on Multi-fractal Properties of Texture Features

Peng Jia[1,2,3], Yi Huang[1], Bojun Cai[1], and Dongmei Cai[1]

[1] College of Physics and Optoelectronics, Taiyuan University of Technology, Taiyuan, 030024, People's Republic of China; robinmartin20@gmail.com

[2] Department of Physics, Durham University, South Road, Durham DH1 3LE, UK

[3] Key Laboratory of Advanced Transducers and Intelligent Control Systems, Ministry of Education and Shanxi Province, Taiyuan University of Technology, Taiyuan, 030024, People's Republic of China

Received 2019 April 1; revised 2019 July 25; accepted 2019 July 26; published 2019 August 19

Abstract

Texture is one of the most obvious characteristics in solar images and it is normally described by texture features. Because textures from solar images of the same wavelength are similar, we assume that texture features of solar images are multi-fractals. Based on this assumption, we propose a pure data-based image restoration method: with several high-resolution solar images as references, we use the Cycle-Consistent Adversarial Network to restore blurred images of the same steady physical process, in the same wavelength obtained by the same telescope. We test our method with simulated and real observation data and find that our method can improve the spatial resolution of solar images, without loss of any frames. Because our method does not need a paired training set or additional instruments, it can be used as a post-processing method for solar images obtained by either seeing-limited telescopes or telescopes with ground-layer adaptive optic systems.

Key words: atmospheric effects – Sun: general – techniques: image processing

Supporting material: animation

1. Introduction

The imaging process of optical telescopes can be modeled by Equation (1):

$$\mathrm{Img}(x, y) = \mathrm{Obj}(x, y) * \mathrm{PSF}(x, y) + \mathrm{Noise}(x, y), \qquad (1)$$

where Obj(x, y) and Img(x, y) are the original and observed images, $*$ is the convolutional operator, PSF(x, y) is the point-spread function (PSF) of the whole optical system, and Noise(x, y) stands for the noise from the background and the detector. During real observations, many different effects will introduce variable PSF(x, y) and Noise(x, y). These effects make the Img (x, y) different from the Obj(x, y), and makes further scientific research difficult.

For ground-based solar observations, because the exposure time is short (dozens of milliseconds) and the field of view is large (compared to the isoplanatic angle), the atmospheric turbulence, thermal, and gravity deformations of the optical system will introduce PSF(x, y) with highly spatial and temporal variations. Even with the help of adaptive optics and active optics systems, the residual error will still introduce a variable PSF(x, y). The variable PSF of solar images is different from that of ordinary nighttime astronomy observations; it is often called short-exposure PSF, because the exposure time is only dozens of milliseconds. The short-exposure PSF cannot be described by any of the contemporary analytical PSF models, such as the Moffat or the Gaussian model, and it is the main limitation for ground-based solar observations.

Several different image restoration methods have been proposed to reduce the effects created by the short-exposure PSF and increase the spatial resolution of astronomical images, such as the blind deconvolution algorithm (Jefferies & Christou 1993), the speckle reconstruction algorithm (Labeyrie 1970; von der Luehe 1993), the phase diversity algorithm (Paxman et al. 1992, 1996; Löfdahl & Scharmer 1994), and the multi-object multi-frame blind deconvolution algorithm (van Noort et al. 2005). These methods have different hypotheses or prior values of the PSF(x, y) or the Img(x, y), including wavefront measurements or assuming that the image is invariant between different frames, and have achieved remarkable performance.

Texture is fundamental characteristic of an image and it describes the grayscale spatial arrangement of images. Normally, texture features are used to evaluate textures. In our recent paper (Huang et al. 2019), we have presented the multi-fractal properties of texture features in solar images of different wavelengths. Based on the results of that paper, in this Letter we use a Cycle-Consistent Adversarial Network (CycleGAN) to restore solar images with multi-fractal properties as regularized conditions. Our method can restore an arbitrary number of solar images obtained by the same telescope within a few days with only several high-resolution images as references. We discuss the multi-fractal property of texture features in Section 2 and introduce our method in Section 3. In Section 4, we show the performance of our method with real and simulated observation data. We make our conclusions and anticipate our future work in Section 5.

2. The Multi-fractal Property of Texture Features In Solar Images

Textures are mostly related to spatially repetitive structures that are formed by several repeating elements (Castelli & Bergman 2002). Similar to other natural images, solar images also have a lot of textures, such as the granulation in TiO and the filament in H-alpha, as shown in Figure 1. The texture feature is a description of the spatial arrangement of the grayscale in an image, and it is usually used to describe the regularity or coarseness of an image. Manually designed texture features have been successfully used to describe the arrangement of texture constituents in a quantitative way (Tamura et al. 1978; Manjunath & Ma 1996; Li-wen et al. 2019). However, textures in solar images are not arranged in a regular or periodic way, which makes it hard to design adequate

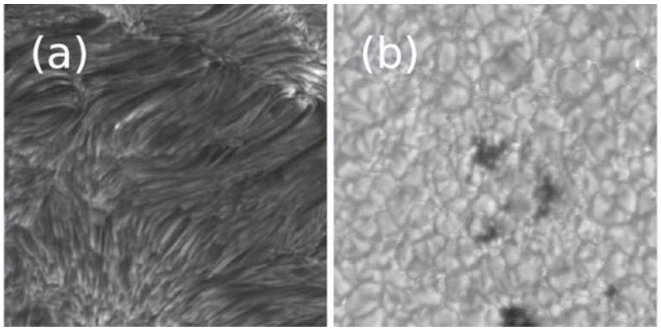

Figure 1. Examples of high-resolution solar images obtained by (a) H-alpha and (b) TiO filters of the New Vacuum Solar Telescope (NVST). In addition to the large structures, there are also a lot of textures in these images. It is easy to tell the difference between images from these two wavelengths, because the textures in each wavelength are relatively stable and high-resolution observations are carried out by humans.

texture features by hand. According to our experience, textures in solar images have the following properties.

1. In the same wavelength, textures from different solar images are similar.
2. For the same solar image, the shape variation of textures in the same spatial scale satisfies the same statistical law. For example, filaments are bending with a smooth curve instead of a polyline.

These properties indicate that although texture features are not organized in a regular way for solar images, the relative weights of different texture features are stable. This means that if we measure the relative weights of texture features in a statistical way, the probability distribution in the same wavelength should be the same. We can use multi-fractal properties to describe texture features in solar images (Jia et al. 2014; Peng et al. 2017). The multi-fractal property of texture features means that the spatial distribution of textures in solar images (coded by texture features) satisfies the same continuous power spectrum, and that the exponents of the spectrum are different for different scales.

Because textures are just images of the background physical process and because the physical process that generates the textures does not change, the multi-fractal properties of texture features are valid for all solar images obtained in the same wavelength; i.e., the texture features of solar images in the same wavelength satisfy the same power spectrum. Recent works suggest that neural networks are very good at representing complex functions.

In this Letter, we try to take further advantage of this property and propose using neural networks to evaluate multi-fractal properties from solar images. The multi-fractal properties are encoded in a neural network and can be visualized by feature maps of each layer. In our recent paper (Huang et al. 2019), we show the multi-fractal properties of G-band images. In this Letter, the multi-fractal properties are used as a regularized condition of the CycleGAN in the same way as other regularization conditions have been used in traditional deconvolution algorithms such as the total variation condition in deconvolution algorithms. Therefore, we do not try to extract the multi-fractal property of texture features directly; instead, we use a number of high-resolution images to represent it in a statistical way.

In real observations, we can obtain numerous high-resolution solar images through speckle reconstruction, phase diversity, multi-object multi-frame deconvolution, or observations with diffraction-limited adaptive optic systems such as the single-conjugate or multi-conjugate adaptive optics systems (Rao et al. 2018). The spatial resolution of these images are around the diffraction limit of the telescope and can reveal the highest spatial frequency of the observation data. As the texture features from high-resolution solar images are just the realization of the theoretical multi-fractal property, we can use the multi-fractal properties of texture features from high-resolution images as a restriction condition for image post-processing methods, as we will discuss in the next section.

3. The CycleGAN for Image Restoration with the Multi-fractal Property

3.1. Introduction of the CycleGAN

The deep convolutional neural network (DCNN) is a type of deep-learning framework and is widely used in image restoration (Xu et al. 2014; Wieschollek et al. 2016; Zhang et al. 2017). For solar images, several different DCNNs have been proposed for image restoration or enhancement (Asensio Ramos et al. 2018; Díaz Baso & Asensio Ramos 2018). These methods are based on supervised learning, which requires pairs of high-resolution images and blurred images as training set to model the degradation process, i.e., the PSF(x, y). However, for real observations, obtaining the training set is difficult, and the number and diversity of images in the training set are usually not large enough to represent different image degradation processes. A trained DCNN will output unacceptable results, when blurred images have a different PSF(x, y) than that of the training set. The requirement of many paired images in the training set limits the wider application of these image restoration methods.

The generative adversarial network (GAN) is a generative model (Goodfellow et al. 2014) that contains two DNNs: a generator G and a discriminator D. Given the real data set R, G tries to create false data that looks like the genuine data from R, while D tries to discriminate the false data and the genuine data. The GAN can be effectively trained with the back-propagation algorithm when there are only limited training data. For the image restoration of galaxies, the GAN has been successfully trained with only 4105 pairs of training images (Schawinski et al. 2017). However, as discussed above, the GAN also models the degradation process from these training images. For solar observations, because the atmospheric-turbulence-induced short-exposure PSF is much more complex than the long-exposure PSF, the number of training images required in the GAN will be greatly increased and the performance of GAN will be strongly influenced by limited training data.

Limited training data is also a problem for other image-related tasks. Zhu et al. (2017) proposed the CycleGAN to solve this problem. The CycleGAN is an unsupervised learning algorithm that contains a pair of GANs. Given two sets of images, one GAN learns the image mapping and the other GAN learns the inverse mapping. Under the constrain condition that the mapped image after inverse mapping should be similar to itself and vice versa (cycle consistency loss), the CycleGAN can restore blurred images directly by using high-resolution images as references. It should be noted that, although the supervised DCNN, the GAN, and the CycleGAN all try to learn the restoration function, when used for image restoration the CycleGAN has very different hypothesis than that of the other methods. The CycleGAN is constrained by the probability distribution of data (multi-fractal property of texture

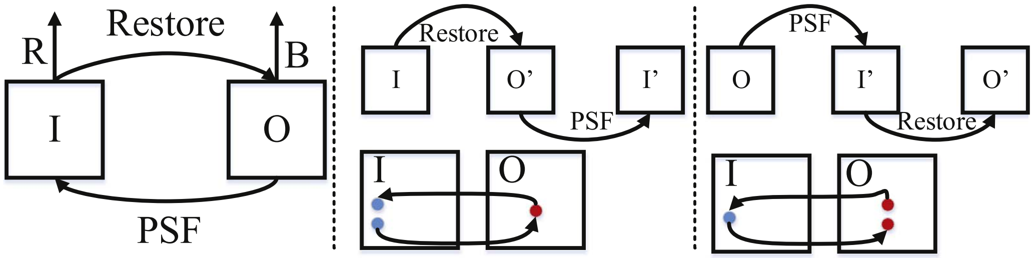

Figure 2. Architecture of the CycleGAN used in this Letter. The left figure shows the basic structure of CycleGAN. I stands for the observation image and O stands for the reference high-resolution image. Restore and PSF stand for the two functions to be learned: the restore function and the PSF. D_I and D_O are two discriminators that are used to evaluate the generator output. The middle and right figures stand for the two learning processes in the CycleGAN. The blue dots are blurred images and the red dots are high-resolution images. The CycleGAN will restore I to O' and then will blur O' to I' and vise versa from O to O'. The cycle consistency loss is introduced to make sure that the above translation will not change the image.

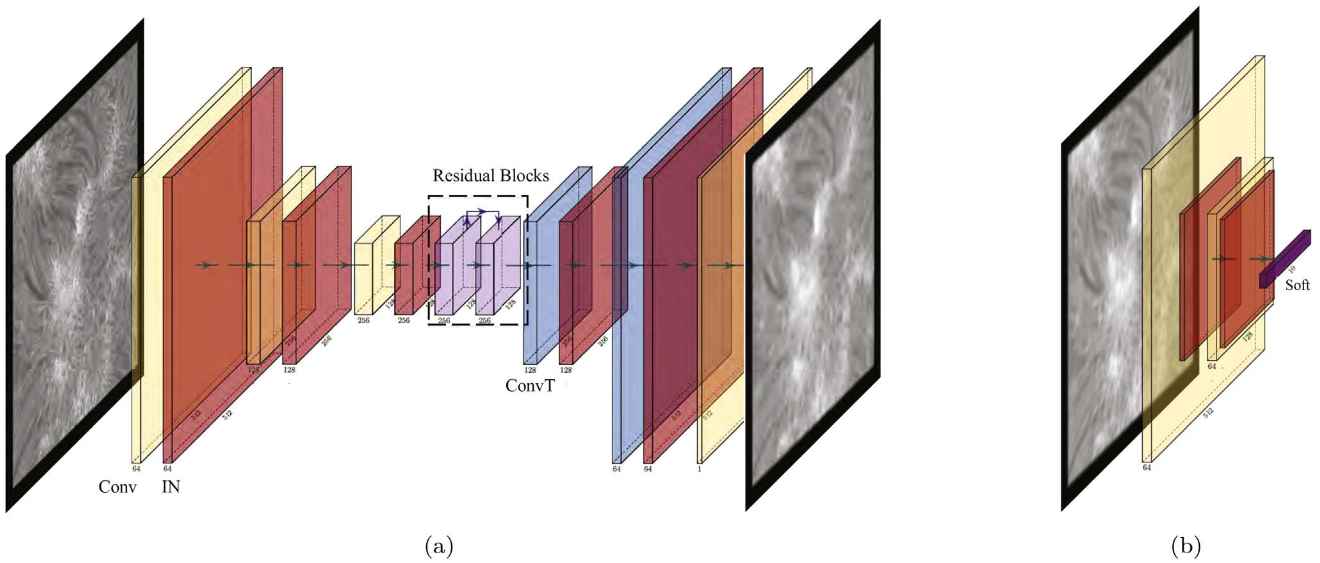

Figure 3. Architecture of the generator in figure (a) and the discriminator in figure (b). The generator is shown in Figure (a), which consists of convolutional layers (Conv in yellow), instance normalization layers (IN in red), Conv-transpose layers (convT in blue), and residual blocks (residual blocks in purple). The discriminator is shown in figure (b), which consists of convolutional layers, instance normalization layers, and softmax layers (in dark purple). The high-resolution image O will be transformed to the blurred image I through the generator and the blurred image will be sent to the discriminator D_I for discrimination. There are two of sets of the generator and the discriminator in the CycleGAN, and they have the same structure.

features in this Letter), while other methods are constrained by the blur properties contained in pairs of training images. The detailed structure of the CycleGAN used in this Letter will be discussed in the next subsection.

3.2. Structure of the CycleGAN for Solar Image Restoration

The structure of the CycleGAN used in this Letter is shown in Figure 2.[4] Because short-exposure PSFs for solar observation have a very complex structure, we use a very deep CNN as a generator as shown in Figure 3 and the Appendix. The residual block in Table 1 (Appendix) is defined in Table 2 (Appendix). This generator is inspired by Zhu et al. (2017). However, because the CycleGAN will learn the short-exposure PSF that has complex structures, we modify it and use smaller convolution kernels here to increase its representation ability. For the discriminator, we use an ordinary CNN that is normally used in image style transfer (Isola et al. 2017; Yi et al. 2017; Zhu et al. 2017) as shown in Table 3 in the Appendix.

As shown in Figure 2, I and O are blurred images and high-resolution images. One GAN in the CycleGAN tries to learn the restoration function and it has a generator Restore and a discriminator D_O, which can be written as: Restore: $I \rightarrow O$. The other GAN tries to learn the PSF and it has a generator PSF and a discriminator D_I, which can be written as PSF: $O \rightarrow I$. We apply ordinary adversarial loss to both of these two GANs as

$$\mathcal{L}_{\mathrm{GAN}}(\mathrm{Restore}, D_O, I, O) = \mathbb{E}_{O\sim p_{\mathrm{data}}(O)}[\log D_O(O)] + \mathbb{E}_{I\sim p_{\mathrm{data}}(I)}[\log(1 - D_O(\mathrm{Restore}(I)))], \tag{2}$$

$$\mathcal{L}_{\mathrm{GAN}}(\mathrm{PSF}, D_I, I, O) = \mathbb{E}_{I\sim p_{\mathrm{data}}(I)}[\log D_I(I)] + \mathbb{E}_{O\sim p_{\mathrm{data}}(O)}[\log(1 - D_I(\mathrm{PSF}(O)))], \tag{3}$$

where $\mathbb{E}_{I\sim p_{\mathrm{data}}(I)}$ stands for the expectation in the probability space of data(I) and vise versa. These two adversarial losses can make the distribution generated by the above two generators close to the real distribution of I or O. However, because the generator is very complex, with the adversarial loss the generator would learn other mappings that also match the distribution of I or O. To further restrict the space of possible mapping functions, we use the cycle consistency loss $\mathcal{L}_{\mathrm{cyc}}(\mathrm{Restore, PSF})$ to constrain the

[4] The complete code used in this Letter is written in Python programming language (Python Software Foundation) with the package Pytorch and can be downloaded from 10.12149/101006.

solution space:

$$\begin{aligned}\mathcal{L}_{\text{cyc}}(\text{Restore, PSF}) &= \mathbb{E}_{O\sim p_{\text{data}}(O)}\\ &\times [\|\text{Restore}(\text{PSF}(O)) - O\|_1]\\ &+ \mathbb{E}_{I\sim p_{\text{data}}(I)}[\|\text{PSF}(\text{Restore}(I)) - I\|_1], \qquad (4)\end{aligned}$$

where $\| \|_1$ stands for the 1-norm. The cycle consistency loss guarantees that, for each image, the CycleGAN will bring it back to the original value:

$$O \rightarrow \text{PSF}(O) \rightarrow \text{Restore}(\text{PSF}(O)) \approx O \qquad (5)$$

$$I \rightarrow \text{Restore}(I) \rightarrow \text{PSF}(\text{Restore}(I)) \approx I. \qquad (6)$$

Because the image restoration algorithm should not flip the gray value between different pixels, we use the identity loss to constrain the contrast of the image, preventing the rapid change of grayscale between different pixels.

$$\begin{aligned}\mathcal{L}_{\text{identity}}(\text{Restore, PSF}) &= \mathbb{E}_{O\sim p_{\text{data}}(O)}[\|\text{PSF}(O) - O\|_1]\\ &+ \mathbb{E}_{I\sim p_{\text{data}}(I)}[\|\text{Restore}(I) - I\|_1] \qquad (7)\end{aligned}$$

Finally, we calculate the total variation of O and I and use them as the total variation loss to improve the image quality and reduce the artifacts generated by the CycleGAN,

$$\begin{aligned}\mathcal{L}_{TV}(\text{Restore, PSF}) &= \mathbb{E}_{I\sim p_{\text{data}}(I)}\\ &\times [\|\nabla_h \text{Restore}(I)\|_2 + \|\nabla_w \text{Restore}(I)\|_2)]\\ &+\mathbb{E}_{O\sim p_{\text{data}}(O)}[\|\nabla_h \text{PSF}(O)\|_2 + \|\nabla_w \text{PSF}(O)\|_2)], \qquad (8)\end{aligned}$$

where $\| \|_2$ stands for the 2-norm, and ∇_{h} and ∇_{w} are horizontal and vertical gradient of these images, respectively. We calculate the weighted summation of the above loss functions and use the function defined below to train the CycleGAN, where λ is the relative weight of the cycle consistency loss.

$$\begin{aligned}\mathcal{L}(\text{Restore, PSF}) &= \mathcal{L}_{\text{GAN}}(\text{Restore}, D_O, I, O)\\ &+ \mathcal{L}_{\text{GAN}}(\text{PSF}, D_I, I, O) + \lambda\mathcal{L}_{\text{cyc}}(\text{Restore, PSF})\\ &+ \mathcal{L}_{\text{identity}}(\text{Restore, PSF}) + \mathcal{L}_{TV}(\text{Restore, PSF}). \qquad (9)\end{aligned}$$

3.3. Other Restriction Conditions for the CycleGAN in Image Restoration

Because the CycleGAN tries to model the degradation process according to the statistical probability distribution of texture features in images, the restriction of this model should lie in both the image and degradation processes. First of all, as the CycleGAN does not have any paired training images as supervisions and it is supervised in the form of O and I, where O and I are high-resolution images and blurred images, respectively, they should satisfy the following properties for O.

1. High-resolution images need to have the same or smaller pixel scale than that of the blurred images. Then we can down sample all the high-resolution images to images of the same pixel scale as that of blurred images in data set O.
2. The apparent structures should be removed from high-resolution images, albeit keeping it small enough, because the apparent structures, such as sunspots, have different textures and will change the multi-fractal properties.
3. We need enough images with textures to represent the multi-fractals in a statistical way. According to our experience, at least 100 frames of reference images with 256 × 256 pixels are required; however, it is much smaller than the ordinary DNN-based image restoration method.

As the CycleGAN is to model the restoration function and the PSF, which have very strong spatial and temporal variations, we need to set several restrictions in I to make the CycleGAN robust in real applications.

1. When restoring a single frame of a solar image, it would be better to divide it into smaller images the size of around dozens of arcseconds.
2. For several continuous frames of solar images, it would be better to cut the interested areas (the size of around dozens of arcseconds) from these images and directly restore these temporal-continuous small images with the CycleGAN.
3. To reduce image processing time, it would be better to use texture-rich small images that are cut from blurred images to train the CycleGAN. After training, the Restore can be directly used to restore all the blurred images.

Last but not least, reference images and blurred images need to have the same multi-fractal property, so the images taken in the same wavelength band within a few days is strict enough for our method. We tested our method with real observation data and found that the neural network used in this Letter is complex enough for the image restoration task, because we did not find any images that the CycleGAN had failed to restore. With the above restrictions, the CycleGAN can be effectively trained through several thousand iterations. In the next Section, we present implementations of our algorithm.

4. Implementations of the CycleGAN for Image Restoration

4.1. Performance Evaluation with Simulated Observation Data

Overfitting is a major problem that can limit the performance of our algorithm. Because the CycleGAN is a generative model, overfitting will make Restore remember the structure of high-resolution images and generate false structures during image restorations. To test our algorithm, we use the CycleGAN to restore simulated blurred images. There are two sets of images used in this Letter: observations carried out in the H-alpha wavelength between 2018 April 2 and 3, and observations carried out in TiO band on 2014 November 17. These two sets of data are both observed by the NVST (Liu et al. 2014): the H-alpha data was observed in 656.28 nm and bandpass of 0.025 nm with a pixel scale of 0.″136 and the TiO data was observed in 705.8 nm and bandpass of 1 nm with with a pixel scale[5] of 0.″052. These images are restored by speckle reconstruction methods (Li et al. 2015).

From five high-resolution H-alpha wavelength images, we crop 500 images of 256 × 256 pixels as references and crop another five images of 256 × 256 as test images. From five high-resolution TiO solar images, we crop 500 images of 256 × 256 pixels as references and crop another five images of 256 × 256 pixels as test images. According to real observation conditions, we use the Monte Carlo method to simulate several high-fidelity atmospheric turbulence phase screens with D/r_0 of 10 for H-alpha wavelength and four for TiO data (Jia et al. 2015a, 2015b), where D stands for the diameter of telescope and r_0 stands for the coherent length of atmospheric turbulence. We calculate simulated short-exposure PSFs with these phase

[5] For more details, please refer to http://fso.ynao.ac.cn/cn/introduction.aspx?id=8.

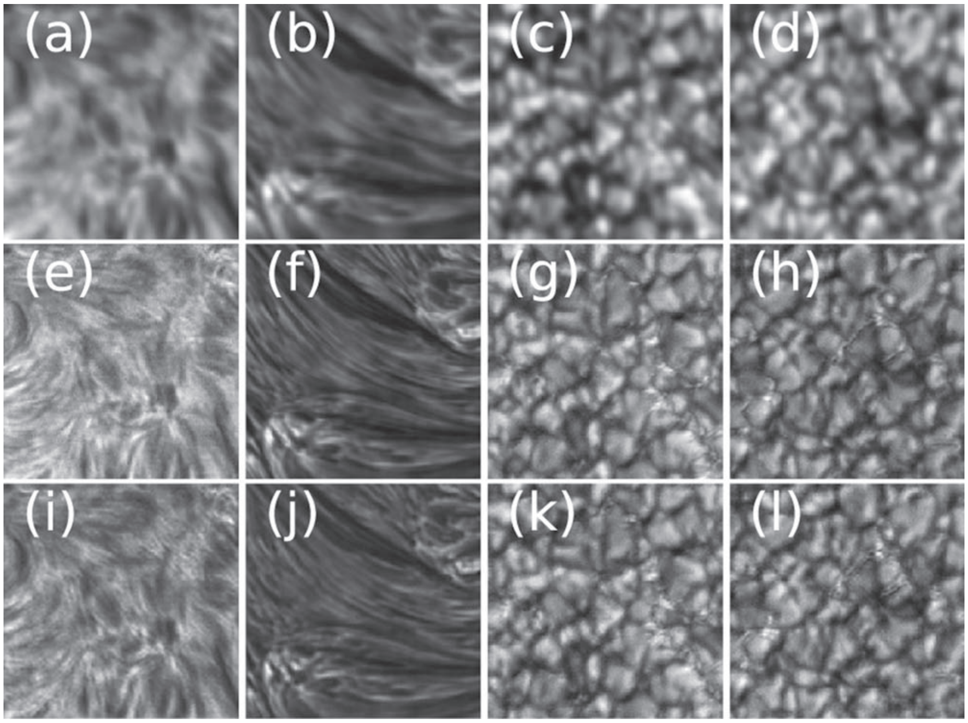

Figure 4. Simulated short-exposure images, restored images, and the original high-resolution images. The figures in the top row show the simulated blurred images, the figures in the middle row show the original high-resolution images, and images in the bottom row show the images restored by our method. The left two columns are images in the H-alpha wavelength, and the right two columns are images in TiO. From these figures, we can find the spatial resolution is increased by our method and, compared with the original high-resolution images, there are no obvious artefacts in the restored images.

screens through far field propagation (Basden et al. 2018). At last, we convolve test images and temporal-continuous PSFs to generate 100 simulated blurred images as simulated blurred H-alpha and TiO data.

These simulated blurred images and high-resolution images in the same wavelength are used to train the CycleGAN with 2000 iterations. Because all of the simulated blurred images have the original high-resolution images, we can compare them to test our algorithm. The results are shown in Figure 4. We carefully check these images and find that the resolution of the restored images has been improved and there are no observable difference between the restored images and the original images. We have also calculated the median filter-gradient similarity (MFGS; Deng et al. 2017) of the simulated blurred images, the original high-resolution images, and the restored images to further test our method. For H-alpha data, the MFGS is increased from 0.75 ± 0.05 to 0.81 ± 0.04, while the mean MFGS of the original images is 0.81 ± 0.04. For TiO data, the mean MFGS is increased from 0.81 ± 0.03 to 0.82 ± 0.02, while the mean MFGS of the original images is 0.82 ± 0.03. According to these results, we find that the image quality has been increased by our method.

4.2. Performance Evaluation with Real Observation Data

In this section we use real observation data from NVST to evaluate performance of the CycleGAN and also show our recommendations of how to use the CycleGAN in real applications. According to the size of the isoplanatic angle, an image should be cut into small images for restoration. However, considering the processing speed we use images with 256 × 256 pixels (equivalent to around 0.5 × 0.5 arcmin) for restoration. This is much larger than the isopanatic angle and the restoration results will decrease slightly; however this trade-off is necessary. In real applications, there are two types of image restoration: the restoration of several continuous solar images in a small interested region or restoration of a single-frame relatively large image.

For the first scene, we use both H-alpha images observed between 2018 April 2 and 3 and small TiO images observed on 2017 August 19 to test our algorithm. For each wavelength, 500 frames of images with 256 × 256 pixels are extracted from five frames of blurred images with 1024 × 1024 pixels, as I and 500 frames of images with 256 × 256 pixels are extracted from one speckle-reconstructed image with 1024 × 1024 pixels as O. Because the CycleGAN is deep and complex, the maximal number and size of the reference image and the blurred image are actually limited by the computer.[6] After training, we can use the Restore to directly restore two interested regions with 256 × 256 pixels in the blurred images. It takes around 1 minutes to process 333 frames of these blurred images. Two frames of restored images are shown in Figure 5 and interested readers can also find animated versions of these figures in the online version of this Letter. They are 100 frames of blurred solar images from H-alpha and 79 frames from TiO before and after restoration, alone with their MFGS values. From these figures, we find that the resolution of the restored images have been improved. The mean MFGS is increased from 0.65 ± 0.01 to 0.89 ± 0.004 for TiO data and from 0.75 ± 0.03 to 0.89 ± 0.007 for H-alpha data.

For the second scene, we test the performance of our algorithm in large images. A blurred image from the NVST is shown in the left panel of Figure 6. The validation part is the

[6] In this Letter, we use a computer with two Nvidia GTX 1080 graphics cards, 128 GB memory, and two Xeon E5 2650 processors. It will cost 4498 s to train the CycleGAN with 6000 iterations.

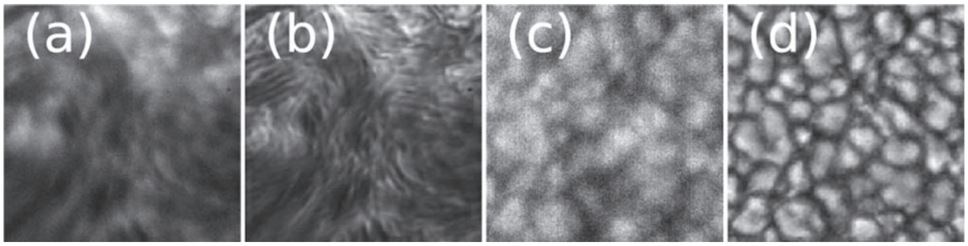

Figure 5. Two frames of real observation images and their corresponding restored images. The two left panels are from the H-alpha wavelength, and the two right panels are from TiO. It is obvious that restored images have better quality. An animated version of this figure is available. In the animation the H-alpha portion is on top, while the TiO sequence is on the bottom. The video duration is 25 s.

(An animation of this figure is available.)

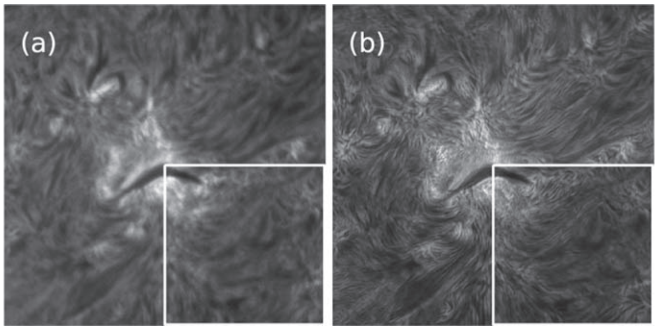

Figure 6. Two frames of real observation images and their corresponding restored images. The size of these two images is 1024 × 1024 pixels. It is obvious that restored images have a higher spatial resolution. The MFGS is increased from 0.78 to 0.89 ± 0.003 in the reference region and the MFGS in the test region of the restored image is 0.89.

image in the white box, and the rest of this image is used as the training part. We extract 500 frames of images with 256 × 256 from the training part as *I*, and use 500 frames of high-resolution images used above as *O* in the CycleGAN. After 6000 iterations, the images in *I* are restored and we use Restore to restore images in the white box. The results are shown in the right panel of Figure 6. We find that the spatial resolution of the observed images has been improved and the difference in image quality between the validation part and the training part is very small. The MFGS is increased from 0.78 to around 0.89 for this image.

5. Conclusions

As more and more high-resolution solar images are obtained, we propose a pure data-based image restoration method to make better use of these data. We assume texture features of solar images in the same wavelength are multi-fractals and use a deep neural network called CycleGAN to restore blurred images, with several high-resolution images from the same telescope as references. Our method does not need paired images as the training set. Instead, with only several high-resolution images observed in the same wavelength, our method can provide promising restoration results for every frame of real observation data without any additional instruments. We use simulated blurred images to test our algorithm. We compare the reconstructed images with real images and find that the MFGS has been increased with our method. In addition, we also use our algorithm to restore real observation images. Although the image quality increased by our method is slightly smaller than the speckle-reconstructed images, our method can restore every frame of blurred images, while the speckle-reconstructed method use a lot of blurred images (dozens or hundreds) and only obtains one frame of restored image. Our method is suitable for future observation data obtained by seeing-limited telescope or telescopes with ground-layer adaptive optic systems. Because our method does not have any prior assumption of the degradation process, it can also be used to restore images of other astronomical objects with features, such as galaxies, nebulae, or supernova remnants.

The authors are grateful to the anonymous referee for comments and suggestions that have greatly improved the quality of this manuscript. The authors would like to thank Dr. Yongyuan Xiang and Professor Kaifan Ji from Yunnan Astronomical Observatory for their suggestions and for providing solar observation data from the NVST. P.J. would like to thank Professor Hui Liu and Professor Zhong Liu from Yunnan Observatory, Professor Yong Zhang from Nanjing Institute of Astronomical Optics and Technology, Dr. Alastair Basden, Dr. Tim Morris, Dr. James Osborn, and Dr. Matthew Townson from Durham University, Dr. Yang Guo and Dr. Qi Hao from Nanjing University, and Dr. Qinmin Zhang from Purple Mountain Observatory, who provided very helpful suggestions for this Letter. This work is supported by National Natural Science Foundation of China (NSFC)(11503018), the Joint Research Fund in Astronomy (U1631133) under cooperative agreement between the NSFC and Chinese Academy of Sciences (CAS). P.J. is supported by the China Scholarship Council to study at the University of Durham. The data used in this Letter were obtained by the New Vacuum Solar Telescope in Fuxian Solar Observatory of Yunnan Astronomical Observatory (CAS).

Appendix
Detailed Structure of the CycleGAN

In this Appendix, we will describe the structure of the Generator and the Discriminator in the CycleGAN. The Generator has several residual blocks, which were first introduced by He et al. (2015), to increase its learning ability.

Table 1
Structure of the Generator

Type	Kernel Size\Stride	Output
Conv2d	7 × 7\1	256 × 256 × 64
IN	⋯	256 × 256 × 64
ReLu	⋯	256 × 256 × 64
Conv2d	3 × 3\2	128 × 128 × 128
IN	⋯	128 × 128 × 128

Table 1
(Continued)

Type	Kernel Size\Stride	Output
ReLu	⋯	128 × 128 × 128
Conv2d	3 × 3\2	64 × 64 × 256
ResidualBlock	⋯	64 × 64 × 256
ResidualBlock	⋯	64 × 64 × 256
ResidualBlock	⋯	64 × 64 × 256
ResidualBlock	⋯	64 × 64 × 256
ResidualBlock	⋯	64 × 64 × 256
ConvT2d	3 × 3\2	128 × 128 × 128
IN	⋯	128 × 128 × 128
ReLu	⋯	128 × 128 × 128
ConvT2d	3 × 3\2	256 × 256 × 64
IN	⋯	256 × 256 × 64
ReLu	⋯	256 × 256 × 64
Conv2d	7 × 7\1	256 × 256 × 1

Note. Conv2d is the standard convolutional layer. IN is an instance normalization layer that will normalize each image through $I = (I - \bar{I})/\mathrm{Var}(I)$, where $\bar{I}$ and Var(I) are mean value and variance of I, respectively. ReLu is the activation function. ResidualBlock is special structure of neural network and the input will feed into its output and the first layer as defined in Table 2. ConvT2d is a transposed convolutional layer that will up-sample the input data through learnable weights.

Table 2
Structure of the ResidualBlock

Type	Kernel Size\Stride
Conv2d	3 × 3\1
IN	⋯
ReLu	⋯
Conv2d	3 × 3\1
IN	⋯

Note. All the layers have the same definitions as those in Table 1. The input will feed into the first layer and the output simultaneously (ResidualBlockOUT = OUT + INPUT, where OUT is the output of the last IN layer, INPUT is the input of the ResidualBlock and ResidualBlockOUT is the output of this ResidualBlock).

Table 3
Structure of the Discriminator

Type	Kernel Size\Stride	Output	Negative Slope
Conv2d	4 × 4\2	128 × 128 × 64	⋯
LeakyReLU	⋯	256 × 256 × 64	0.2
Conv2d	4 × 4\2	64 × 64 × 128	⋯
IN	⋯	64 × 64 × 128	⋯
LeakyReLU	⋯	64 × 64 × 128	0.2
Conv2d	4 × 4\1	64 × 64 × 256	⋯
IN	⋯	64 × 64 × 256	⋯
LeakyReLU	⋯	64 × 64 × 256	0.2
Conv2d	4 × 4\1	64 × 64 × 1	⋯
Sigmoid	⋯	⋯	⋯

Note. LeakyReLu is a leakyReLu activation function that has a small slope for negative values, and in this Letter we use the negative slope of 0.2. Sigmoid is the output layer of the discriminator and is used for the classification of the input signals. All other layers have the same definitions as those in Table 1.

ORCID iDs

Peng Jia https://orcid.org/0000-0001-6623-0931

References

Asensio Ramos, A., de la Cruz Rodriguez, J., & Pastor Yabar, A. 2018, arXiv:1806.07150

Basden, A. G., Bharmal, N. A., Jenkins, D., et al. 2018, SoftX, 7, 63

Castelli, V., & Bergman, L. D. 2002, Image Databases: Search and Retrieval of Digital Imagery (New York: Wiley)

Deng, H., Zhang, D., Wang, T., et al. 2017, arXiv:1701.05300

Díaz Baso, C. J., & Asensio Ramos, A. 2018, A&A, 614, A5

Goodfellow, I. J., Pougetabadie, J., Mirza, M., et al. 2014, in Advances in Neural Information Processing Systems, ed. Z. Ghahramani et al., Vol. 27 (Red Hook, NY: Curran Associates, Inc.), 2672

He, K., Zhang, X., Ren, S., & Sun, J. 2015, arXiv:1512.03385

Huang, Y., Jia, P., Cai, D., & Cai, B. 2019, arXiv:1905.09980

Isola, P., Zhu, J., Zhou, T., & Efros, A. A. 2017, CVPR, 2017, 5967

Jefferies, S. M., & Christou, J. C. 1993, ApJ, 415, 862

Jia, P., Cai, D., & Wang, D. 2014, ExA, 38, 41

Jia, P., Cai, D., Wang, D., & Basden, A. 2015a, MNRAS, 447, 3467

Jia, P., Cai, D., Wang, D., & Basden, A. 2015b, MNRAS, 450, 38

Labeyrie, A. 1970, A&A, 6, 85

Li, X. B., Liu, Z., Wang, F., et al. 2015, PASJ, 67, 479

Liu, Z., Xu, J., Gu, B., et al. 2014, RAA, 14, 705

Li-wen, W., Peng, J., Dong-mei, C., & Hui-gen, L. 2019, ChA&A, 43, 128

Löfdahl, M. G., & Scharmer, G. B. 1994, A&AS, 107, 243

Manjunath, B. S., & Ma, W.-Y. 1996, ITPAM, 18, 837

Paxman, R. G., Schulz, T. J., & Fienup, J. R. 1992, JOSA A, 9, 1072

Paxman, R. G., Seldin, J. H., Loefdahl, M. G., Scharmer, G. B., & Keller, C. U. 1996, ApJ, 466, 1087

Peng, F., Zhou, D.-l., Long, M., & Sun, X.-m 2017, AEU-International Journal of Electronics and Communications, 71, 72

Rao, C., Zhang, L., Kong, L., et al. 2018, SCPMA, 61, 089621

Schawinski, K., Zhang, C., Zhang, H., Fowler, L., & Santhanam, G. K. 2017, MNRAS, 467, L110

Tamura, H., Mori, S., & Yamawaki, T. 1978, ITSMC, 8, 460

van Noort, M., Rouppe van der Voort, L., & Löfdahl, M. G. 2005, SoPh, 228, 191

von der Luehe, O. 1993, A&A, 268, 374

Wieschollek, P., Scholkopf, B., Lensch, H. P. A., & Hirsch, M. 2016, in Computer Vision – ACCV 2016, ed. S.-H. Lai et al. (Dordrecht: Springer), 35

Xu, L., Ren, J. S., Liu, C., & Jia, J. 2014, in Advances in Neural Information Processing Systems, ed. Z. Ghahramani et al., Vol. 27 (Red Hook, NY: Curran Associates, Inc.), 1790

Yi, Z., Hao, Z., Ping, T., & Gong, M. 2017, in IEEE International Conference on Computer Vision (New York: IEEE), 2849

Zhang, K., Zuo, W., Gu, S., & Zhang, L. 2017, CVPR, 2017, 3929

Zhu, J., Park, T., Isola, P., & Efros, A. A. 2017, in International Conference on Computer Vision, 2242 (New York: IEEE), 2223